catalysts

MDPI

Article

Synthesis and Characterization of N-Doped SiC Powder with Enhanced Photocatalytic and Photoelectrochemical Performance

Wanli Liu, Qi Li, Xianglong Yang *, Xiufang Chen and Xiangang Xu

State Key Laboratory of Crystal Materials, Shandong University, Jinan 250100, China; lwlsdu@mail.sdu.edu.cn (W.L.); liqi1995@mail.sdu.edu.cn (Q.L.); cxf@sdu.edu.cn (X.C.); xxu@sdu.edu.cn (X.X.)

* Correspondence: yangxl2016@sdu.edu.cn; Tel.: +86-151-6505-7949

Received: 2 June 2020; Accepted: 6 July 2020; Published: 9 July 2020

Abstract: Solar-light-driven N-doped 3C–SiC powder was synthesized via a simple one-step combustion route. SiC–N_2 photocatalysts exhibited 205.3 μL/(g·h) hydrogen evolution rate, nearly 2 times that of SiC–Ar(120.1 μL/(g·h)), and was much higher than that of SiC nanowires (83.9 μL/(g·h)), SiC nanoparticles (82.8 μL/(g·h)) as well as the B-doped SiC photocatalysts(166 μL/(g·h)). In cyclic tests, N-doped SiC also performed excellent photocatalytic durability and good structural stability. It can be concluded that the influence of N-doping introduced defects into the SiC photocatalyst by occupation and mixed phase structure, transformed the band structure into the direct band gap, and formed a shallow donor level for trapping holes. Consequently, higher photocatalytic activities and lower recombination was achieved. Furthermore, the carbon on the photocatalyst which was yielded from the substitution of N or which remained after combustion would build constructed efficient interfacial contact with SiC for the quickening of light-driven electron transfer to the surface, and simultaneously strengthen the adsorption capacity and light-harvesting potential.

Keywords: N-doped; SiC; photocatalysis; hydrogen production

1. Introduction

Confronted with the dual pressures of a resource crisis and environmental pollution, the sustainable development and use of clean energy has become a hot issue [1]. The conversion of solar energy into hydrogen via water-splitting using a semiconductor as a photocatalyst has been considered to be an ideal and promising processes for the generation of clean and renewable energy [2,3].

To date, varieties of materials for photocatalytic application have been widely studied since Fujishima and Honda initially reported photoelectrochemical hydrogen production using TiO_2 [4]. Similar to TiO_2, many other metal oxides are also active for water-splitting, but a wide band gap and low quantum efficiency has a negative impact with regard to the efficient use of sunlight [5]. Non-oxides possess the band gap necessary to absorb visible light, but are generally unstable and prone to photo-corrosion and self-oxidation [6]. Therefore, it is still urgently necessary to develop photocatalysts that can use visible light and that are highly stable, as well as highly efficient and less expensive [7].

Silicon carbide (SiC) had an appropriate and tunable band gap (2.4–3.2 eV) [8] and a relatively negative conduction band position for visible-light-driven photocatalytic hydrogen evolution. Moreover, it exhibits high charge-carrier mobility, excellent thermal and chemical stability, and is environmentally friendly and abundant in low-cost raw materials [9]. However, SiC does not exhibit a satisfying photocatalytic action due to its low hydrogen production efficiency caused by an indirect band gap, lack of active sites, and high recombination rate of photo-excited e^-/h^+ pairs [10,11].

To address these challenges and improve the photocatalytic performance of SiC catalysts, various engineering strategies, such as morphology or structure control [12–14], non-metal doping [15,16], noble metal deposition (Au, Ag, Pt, etc.) [17–19], construction of combination and heterostructures (e.g., TiO_2/SiC [20], SnO_2/SiC [21], MoS_2/SiC [22], SiC/CdS [23–25], g-C_3N_4/SiC [26], and SiC/$BiVO_4$ [27], and hybridization of carbon materials (e.g., carbon nanotubes-SiC, graphene-SiC hybrids, and graphitic carbon-SiC [28–31] have been manufactured. However, the preparation of SiC photocatalyst that is efficient, stable, and visible-light-driven via a simple method remains a challenge. Ion-doping has proved to be a valid and widely used way to improve photocatalytic activity by expanding the light-response range and altering the recombination rate of photo-excited e^-/h^+ pairs. Nitrogen is widely used as an n-type dopant in silicon carbide due to its similarity in atomic radius compared to a C atom. For N-doped SiC, studies have mainly focused on the diffusion of N in SiC [32] and the dielectric and optical properties of N-doped SiC [33]; the effect of N-doping in SiC for photocatalytic H_2 production under visible light has not been reported so far. Along with gradual occupation by N atoms at the C site, Si_3N_4 is also produced as an important intermediate product during the N-doping process. As the crystallization of SiC is hindered by the formation of Si_3N_4, the grain size is lessened, which improves chemical activities. At the same time, the reduction of Si_3N_4 raises the N pressure around the SiC lattice, which urges the occupation of N to form SiCN solid solution and yields graphite C, which enriches the diversity of the phases. The band structure transforms into the direct band gap with band-gap shrinkage due to the capture of unmatched electrons by Si 3p after N substitution. Additionally, separation photoelectron holes, promoted by heterostructure and interfacial contact, form in the photocatalyst.

Herein, a simple combustion synthesis process combining ion-doping and carbon-coating was adopted to prepare N-doped SiC. The as-prepared N-doped 3C-SiC photocatalyst was obtained with an enhanced activity as high as 205.3 μL/(g·h) for H_2 production under solar light, which is nearly 2 times that of SiC–Ar (120.1 μL/(g·h)), and was much higher than that of SiC nanowires (83.9 μL/(g·h)), SiC nanoparticles (82.8 μL/(g·h)), and the B-doped SiC photocatalysts (166 μL/(g·h)). The chemical state, morphology, phase structure, optical properties, and the band structure of N-doped SiC were also investigated to evaluate the impact of N-doping on the photocatalytic activities. The strategy in this work provides a widely used reference for SiC-based systems to improve related photocatalysis.

2. Results and Discussion

2.1. Synthesis and Characterization

The X-ray diffraction (XRD) patterns of the as-prepared samples are shown in Figure 1. The characteristic diffraction peaks at 2θ = 35.8°, 41.3°, and 60° which are indexed as the (111), (200), and (220) facets of cubic SiC (JCPDS, No. 29–1129) appear in both samples, which implies that the main phase structure of SiC does not change significantly after N-doping. For the N-doped sample, the intensities of the peaks mentioned above decrease; additionally, the characteristic peaks of graphite C and Si_3N_4 weakly appear, indicating that the traces of residual carbon and Si_3N_4 appear in the product. This is accompanied by the direct formation (1) of SiC:

$$\mathrm{Si\ (l,\ s) + C\ (s) = SiC\ (s)} \quad (1)$$

Si_3N_4 also came out as an intermediate product as shown in reaction (2),

$$\mathrm{3Si\ (s) + 2N_2(g) = Si_3N_4\ (s)} \quad (2)$$

which not only retarded the generation of SiC owing to its more thermodynamic activity under 1550 °C [34], but also resulted in higher local N pressure in the SiC lattice, which accelerated the occupation by N atoms on C atoms and produced a SiC(N) solid solution. Consequently, the excess C, which is replaced by N, yielded graphite C in the final product. When the carbon was sufficient under

an inert atmosphere and above the boundary temperature 1450 °C, the conversion from Si_3N_4 to SiC would be continuous until complete (3) [35].

$$Si_3N_4\ (s) + 3C = 3SiC\ (s) + 2N_2\ (g) \quad (3)$$

The existence of peaks assigned to graphite C and Si_3N_4 is evidence of the unfinished process.

The detailed enlargement of the peak at 41° corresponding to (200) plane displays a shift towards the higher 2θ angle in the SiC–N_2 sample, compared to SiC–Ar, suggesting a narrowed interplanar distance d, and a consequently reduced lattice constant a. Calculated by Jade 5.0 software, the lattice constant corresponding to 3C–SiC of SiC–N_2 is 4.20 Å, whose value is much smaller than the standard value 4.36 Å of 3C–SiC, which is consistent with the result of the peak shift. The reason for the above change can be summarized as follows: (1) owing to its priority formation below the boundary temperature and drop in the combustion temperature when decomposed, Si_3N_4 restricts the generation of 3C–SiC and weakens its crystallinity; (2) the transformation between Si_3N_4 and SiC urges the occupation by smaller N atoms (radius: 0.080 nm) on C sites (radius: 0.086 nm), and forms the SiC(N) solid solution; (3) along with the substitution of N and further formation of Si–N bonds, a point crystal defect with negative electricity occurs, due to the residual unmatched electrons being captured by Si 3p [36]. The change of lattice constant a is listed in Table 1.

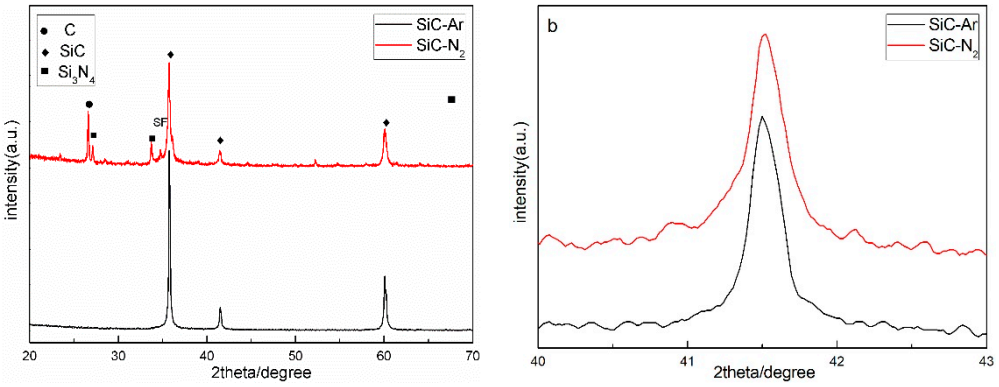

(**a**) (**b**)

Figure 1. (**a**) XRD patterns of SiC–N_2 and SiC–Ar; and (**b**) the magnification of the diffraction peak (200).

Table 1. Characterization results of SiC photocatalysts.

Sample	A/nm	E_g/eV	E_{fb}/V
SiC–Ar	0.436	2.34	−0.47
SiC–N_2	0.420	2.17	−0.29

a: lattice constant; E_g: band-gap energy; E_{fb}: flat band potential.

X-ray photoelectron spectroscopy (XPS) was used to determine the chemical state and surface properties of the catalysts, as shown in Figure 2 and Table 2, which can resolve SiC and Si_3N_4 using distinct binding energies owing to the distinction in the electronegativities of N and C. The component of C 1s at the lowest binding energy (283.2 eV) is due to C–Si bonds [37]. The peak at around 284.8 eV s ascribed to amorphous carbon left after combustion or contaminant carbon. The additional C 1s peaks from 285.2 to 287.1 eV are reported to refer to CNx [38–40]. The N 1s signals obtained from the samples are consistent with the trend of C 1s mentioned above. From the XPS spectra of N 1s (Figure 2e,f), the peak centered at 397.8 eV represents the fraction N–Si, whereas that the peak at 399.9 eV is assigned to N–C. Associated with the C 1s, N–C bonds are expected to come either from SiCN metastable [37] or a reaction between N_2 and free carbon. SiC and CN_x are expected to react as follows:

$$3Si + 2N_2 + 5C \rightarrow 3SiC + 2CN_x + (2 - x)\,N_2 \quad (4)$$

The Si 2p spectra consisted of three peaks—99.7, 101.7, and 103.8 eV—which can be attributed to Si–C, Si–N, and silicon oxide, respectively. On the one hand, the silicon oxide came from the oxygen adsorption during the combustion; on the other hand, the silicon oxide formed as a protective layer on the surface of Si_3N_4 by passivation oxidation [41], so the peak area ratio of Si–O apparently changes with the growth of Si–N amounts. The crystallization of SiC weakened by the formation of Si_3N_4 also can be observed by the contrast to the Si 2p data. Consequently, based on the XPS report, the final product of SiC–N_2 was the mixture of SiC, Si_3N_4, and SiCN nano-ordered structure, whose multiple-phase structure and generated defects would enhance photocatalytic activities.

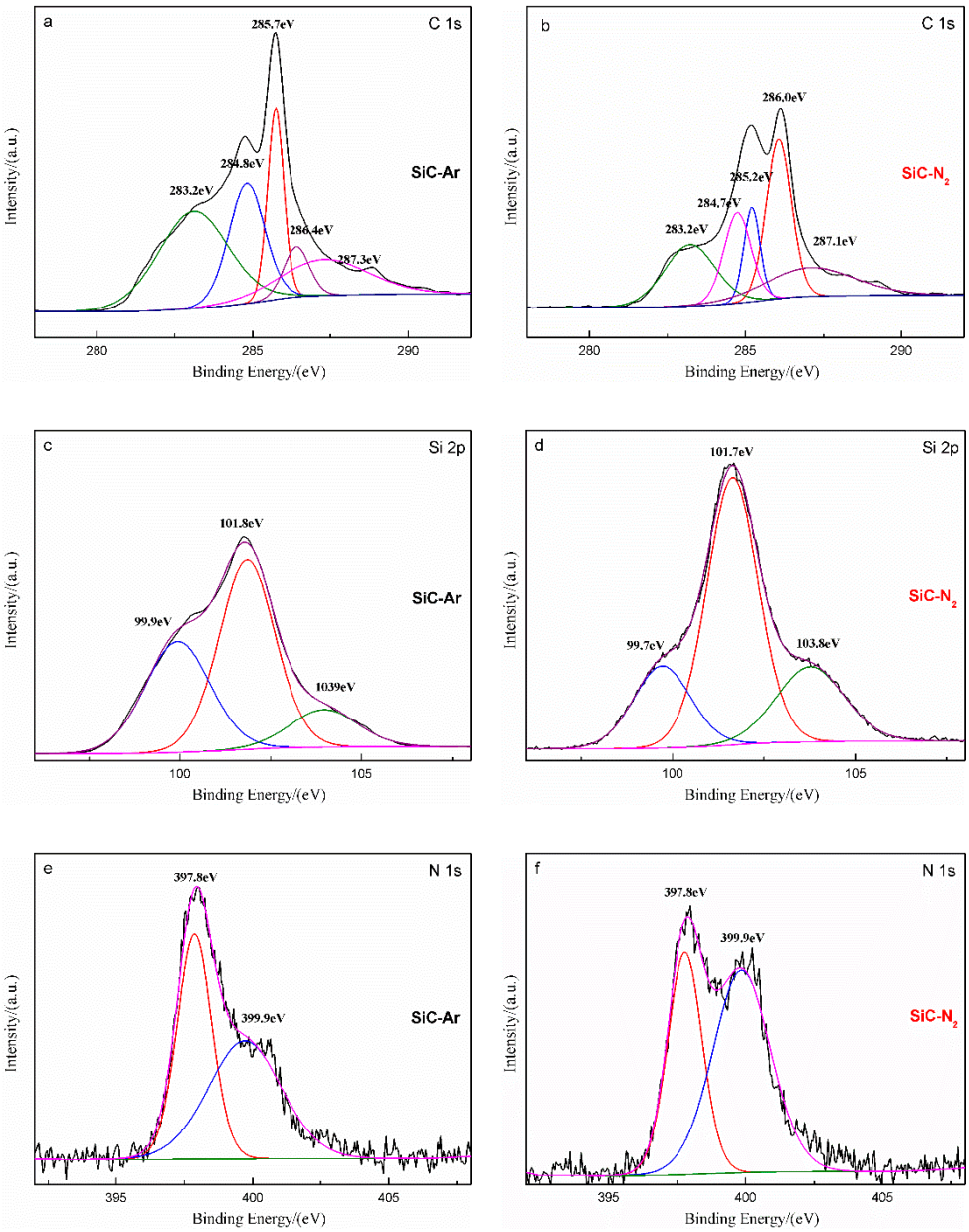

Figure 2. The XPS spectra of C1s (**a**,**b**) Si 2p(**c**,**d**), (**e**,**f**) N 1s.

Table 2. Photoelectron binding energies measured in this experiment.

Composition Spin	Bond	Binding Energy(eV)	Literature(eV)
C 1s	C–Si	283.2	283.4 [37]
	C–C	284.8	284.6 [37]
	CNx	285.2–287.1	285.4–288 [40]
Si 2p	Si–C	99.7	100.3 [41]
	Si–N	101.7	101.9 [37]
	Si–O	103.8	104.1 [37]
N 1s	N–Si	397.8	397.8 [42]
	N–C	399.9	399.0 [37]

Figure 3a,b presents the scanning electron microscopy (SEM) images of the as-prepared samples. It can be seen that both the samples display similar granular structures and morphologies with dissimilar average size of ≈ 100–200 nm and ≈ 200–300 nm for SiC–N_2 and SiC–Ar, respectively. The grain size of the doped samples is obviously smaller with rougher surface compared to the other one. Consistent with the XRD results, the narrowed size is mainly associated with Si_3N_4, which hindered crystallinity. Additionally, the substitution of N atoms into a SiC lattice yields residual carbon, which gathers to shape the rough surface. The Transmission Electron Microscope (TEM) Image in Figure 3c clearly displays the morphology of the SiC–Ar particle with a slippery surface. However, the SiC–N_2 shows a dissimilar appearance whose surface is tightly covered by irregular sheet-like carbon, as shown in Figure 3d. More details about the structure and chemical composition of the samples is given by high-resolution transmission electron microscope (HRTEM) and EDS characterizations. As shown in Figure 3e, the clear lattice fringes with an interplanar lattice spacing of 0.25 nm corresponds to the (111) facet of SiC, whereas the lattice fringes with d spacing of about 0.33 nm can be indexed as the (004) plane of carbon. The interlaced structure of lattice formed by (004) planes of carbon and the (111) planes of SiC indicates the superior contact between them, at which the interfacial interaction plays a key role in photocatalytic activity. Element mapping for N and Si shows that the N element exists uniformly but rarely, which implies the doping of N atoms within the SiC framework using this simple strategy.

To understand the origin of charge separation, optical absorption behavior of the as-prepared samples was investigated by UV-Vis spectroscopy. As is evident in Figure 4a, both photocatalysts had wide photoabsorption; moreover, SiC–N_2 exhibited a notable enhancement of absorption in the visible region (>400 nm), and its absorption edge (592 nm) appeared as a red shift compared with SiC–Ar (535 nm). Based on the widely accepted equation $E_g = 1240/\lambda$, the band-gap energy (E_g) can be estimated at 2.09 eV and 2.32 eV for SiC–N_2 and SiC–Ar, respectively. The band gap can also be calculated more accurately using the following formula:

$$\alpha h\nu = A(h\nu - Eg)^{n/2} \quad (5)$$

where α, h, ν, A, and E_g are the absorption coefficient, Plank constant, photon frequency, proportionality constant, and band-gap energy, respectively. Among them, the value of exponent n was determined by the nature of the transition in the semiconductor ($n = 1$ for a direct transition and $n = 4$ for an indirect transition). From the plot of $(\alpha h\nu)^{n/2}$ vs. $h\nu$ (Figure 4b,c), a good approximation of band-gap energies (E_g) can be obtained from the intersection between the extrapolated linear portion and the baseline. Although the absorption was not steep in the indirect band-gap semiconductor, the intersection with the baseline would be regarded as the E_g [43]. Considering that the type of the transition is unknown, the E_g is calculated on both conditions, as shown in Figure 4b,c. Assuming SiC–Ar to be an indirect band-gap semiconductor, the band-gap energy ($E_g = {}_{\text{indirect}}$) of the as-prepared pure SiC–Ar was 2.34 eV; conversely, the band gap as direct transition ($E_g = {}_{\text{direct}}$) was estimated to be 2.52 eV. For the doped-sample SiC–N_2, the $E_g = {}_{\text{indirect}}$ and $E_g = {}_{\text{direct}}$ was 2.56 eV and 2.12 eV, respectively. By matching

the E_g value with the result concluded from the absorbance, the characteristics of the transition for SiC–Ar was proved to be indirect, and SiC–N_2 had a direct band gap. After N-doping, the band gap was shortened so that the value decreased from 2.34 eV (SiC–Ar) to 2.12 eV (SiC–N_2). The nature of N-doped SiC transforms from an indirect transition to a direct transition with band-gap shrinkage after the C atom is substituted by the N atom, which is also mentioned in previous studies [36]. Mott–Schottky plots were employed to further study the relative position of the band structure after N-doping, as shown in Figure 4c. Both the plots have a linear relationship over the voltage range with positive slopes, which indicates the n-type conductive behavior of the samples. The flat band potentials E_{fb} of SiC–Ar and SiC–N_2 are estimated to be −0.67 and −0.49 V (vs. Ag/AgCl), respectively. It is known that E_{fb} is strongly related to the position of the conduction band (CB) and is considered to be located just below the bottom of the CB in n-type semiconductors. Accordingly, the CB position of SiC–N_2 is down-shifted from −0.47 to −0.29 eV (vs. NHE) compared to SiC–Ar. It is worth mentioning that after N-doping, the characteristic of SiC-N_2 transforms from an indirect transition to a direct transition, and the band gap is reduced due to the CB bottom shifted below. Obviously, SiC–N_2 enhances the photo-absorption properties by adjusting band structure, and shows potential for H_2 production under visible-light irradiation.

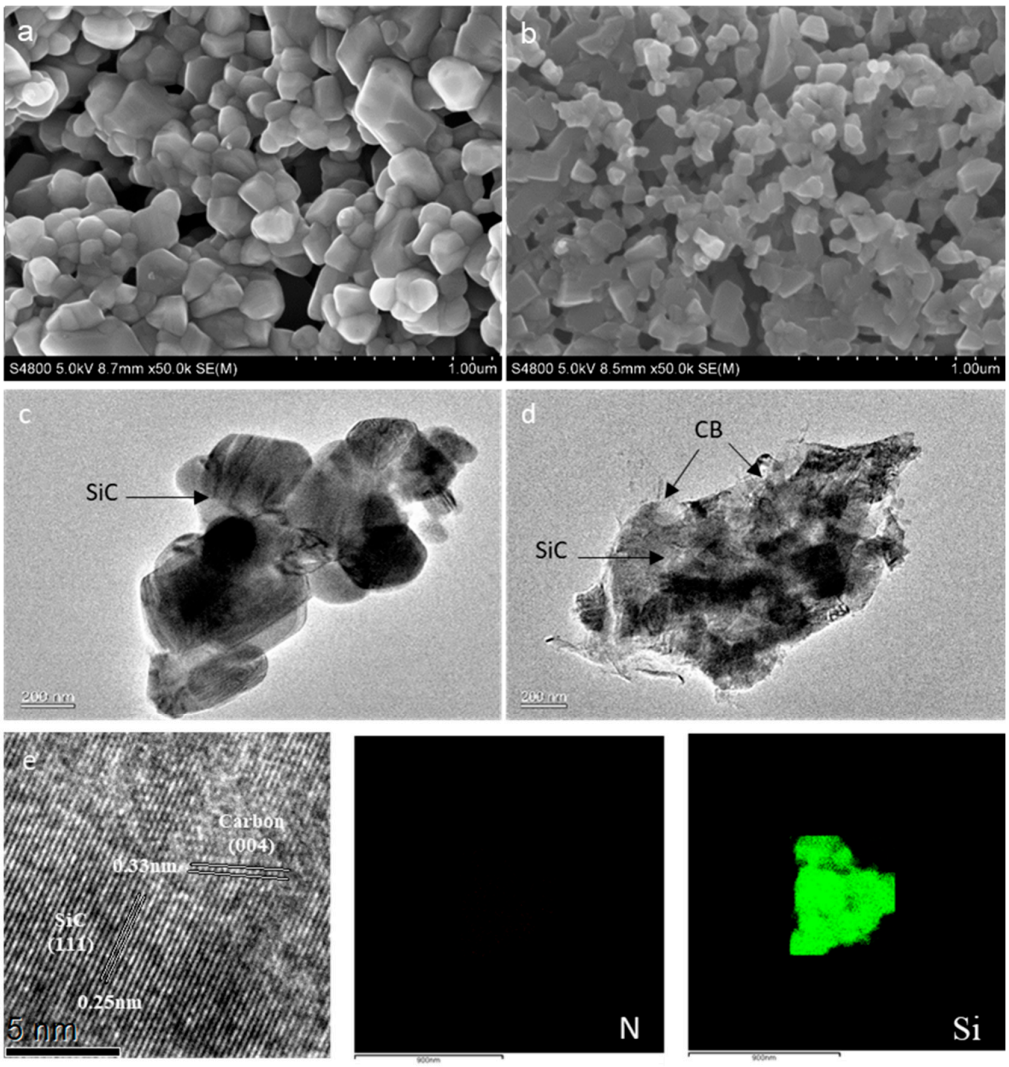

Figure 3. Scanning electron microscopy (SEM) images of SiC–Ar (**a**) and SiC–N_2 (**b**), The high-resolution transmission electron microscope (HRTEM) images of SiC–Ar (**c**) and SiC–N_2 (**d**), corresponding HRTEM and STEM-EDS elemental mapping image of SiC–N_2 (**e**).

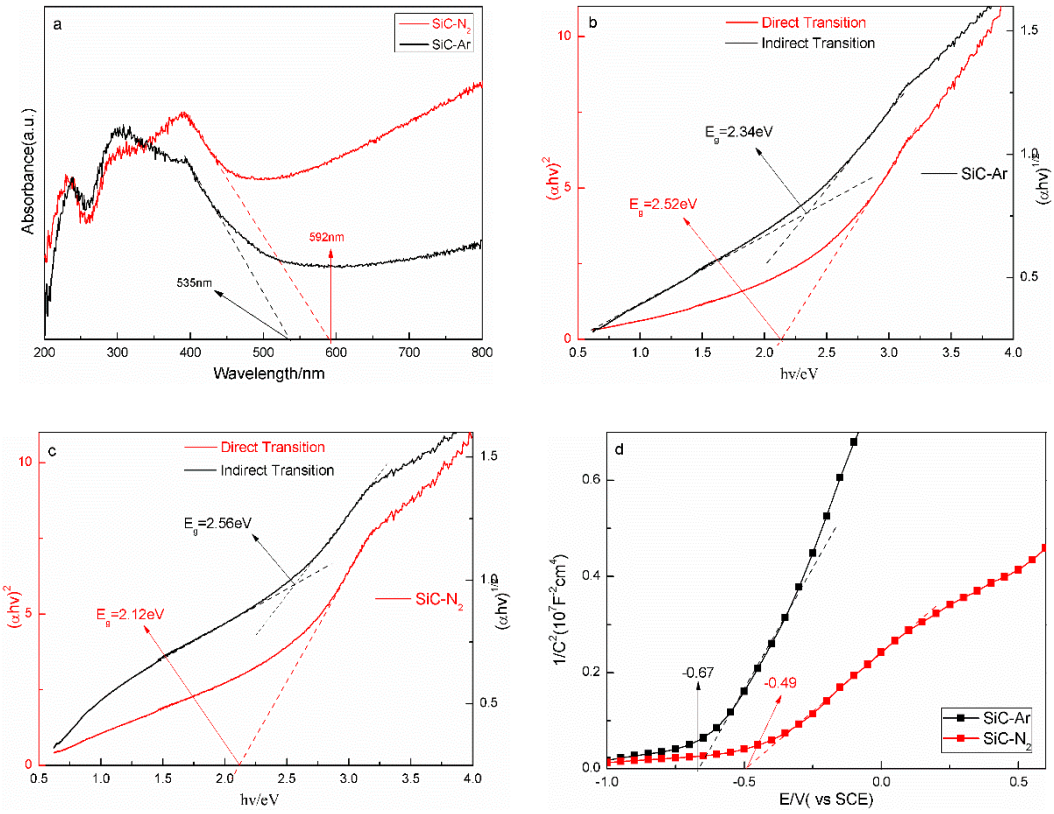

Figure 4. UV-Vis absorption spectra (**a**), plots of $(\alpha h\nu)^{n/2}$ versus hν of SiC–Ar (**b**) and SiC–N_2 (**c**), and Mott–Schottky plots of SiC–N_2 and SiC–Ar in 0.5 mol·L^{-1} Na_2 SO_4 solution (**d**).

2.2. Photocatalytic, Kinetic, and Photoelectrochemical Properties

The photocatalytic properties of SiC–Ar and SiC–N_2 for solar-to-H_2 conversion were assessed in the presence of sacrificial agents under simulated solar light irradiation. The time curve of the produced hydrogen accumulation on the SiC samples is given in Figure 5a, in where it nearly linearly increases in the reaction region, signifying good photochemical stability. No apparent decline of hydrogen evolution is observed in Figure 5b after three repeated runs over 15 h, indicating that SiC–N_2 exhibited satisfactory stability and cyclability during the photocatalytic hydrogen production process. SiC–N_2 exhibited average photoactivity with a rate of (205.3 μL/ (g·h)), which is much higher than that of SiC nanowires (83.9 μL/ (g·h)), SiC nanoparticles (82.8 μL/ (g·h)) [14], or B-doped SiC photocatalysts (166 μL/ (g·h)) [16].

These results can be ascribed to the narrowed band gap, favorable chemical activity, and low recombination of carriers. The residual carbon in the final product not only promotes the light harvest under visible light but also leaves a rougher surface and sharper edges, so that higher specific surface area and a greater number of dangling bonds is achieved. Thanks to the reduced crystallinity, the narrowed grain size increased the reaction area, while the point defects enriched the reaction sites. The reason for the enhancement in separation of light-induced carriers can be outlined as follows: (1) the carriers can be excited easily due to direct band-gap structure, and separated through the heterostructure and interfacial bonding brought on by the mixed phase structure; the photo-induced electrons are further transited to the carbon covering of the SiC and react efficiently with the solution. (2) The defects caused by occupation of the N on the C site in the SiC lattice became the traps that captured the holes, and the recombination of carriers is inhibited.

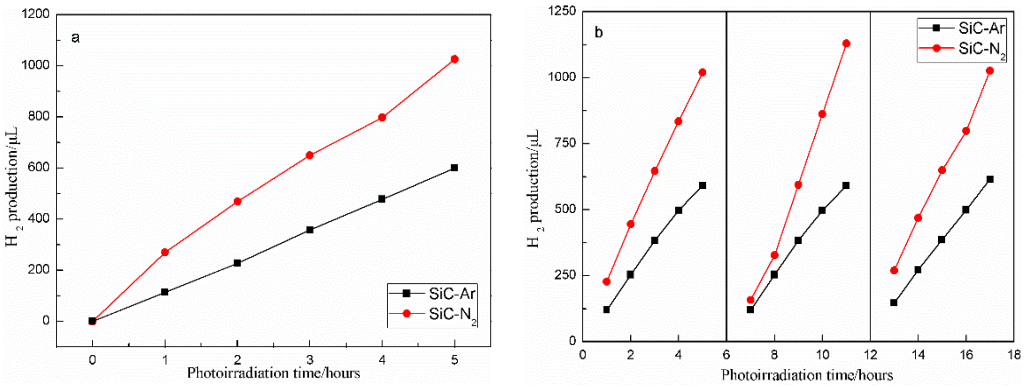

Figure 5. Photocatalytic hydrogen evolution performance (**a**) and cyclic experiments (**b**) of SiC–N_2 and SiC–Ar.

The photo-generated charge separation and migration were validated by photoelectrochemical measurement. As is evident in Figure 6, the transient photocurrent density of SiC–N_2 (about 0.34 μA/cm^2) was nearly twice as big as that of un-doped SiC–Ar (about 0.16 μA/cm^2), revealing an enhanced ability to generate and transfer charges. The improvement of separation efficiency in SiC–N_2 was attributed to the narrowed band gap and the hole trap brought on by N-doping, thereby increasing the solar-light use and decelerating the recombination of photo-generated e^-/h^+ pairs.

To achieve further insight into the transport capability and internal resistances of photocatalysts, electrochemical impedance spectroscopy (EIS) measurement was performed. It can be clearly seen from Figure 6b that N-doping leads to a smaller arc radius on the Nyquist plot as compared to un-doped SiC–Ar, suggesting a lower transfer resistance, and further reflecting a quicker charge transfer and better carrier mobility. The promoted transport performance of photo-induced carriers was achieved in SiC–N_2, owing to the interfacial interaction among the mixed phase structure and the high conductivity offered by carbon-covered photocatalysts.

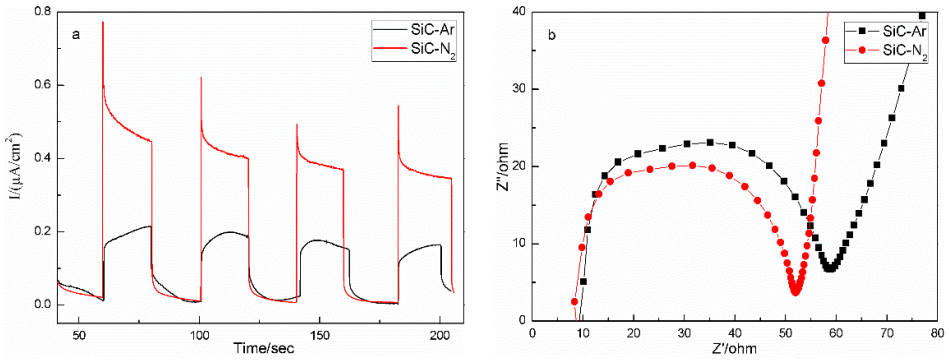

Figure 6. The photocurrent density (**a**) and EIS responses (**b**) of SiC–N_2 and SiC–Ar electrodes.

2.3. Reaction Mechanisms

Here, a feasible mechanism of PHE over SiC–N_2 base on those reported properties above is proposed in Figure 7. Thanks to the narrowed band gap and direct transition, the photo-induced electron-hole in SiC–N_2 was prone to be excited by solar-light irradiation. Owing to the Fermi level of carbon, part of the photo-generated electrons would be injected through the rectifying interface into the carbon surface of the SiC, whose adsorption capacity and chemical activity would accelerate the reaction in solution. Despite the wide band-gap material, Si_3N_4 remained in the SiC–N_2 sample, the excited electrons can transfer to SiC–N_2 via the heterostructure and be involved in the reaction, leaving the holes on the value band to react with the sacrificial agent. The phase transformation forms superior contact among them, where the interfacial interaction plays a key role in the photo-generated

h^+/e^- pair transmission. Additionally, the replacement of the C atom by the N atom would form a shallow donor as hole traps and a crystal defects, preventing the recombination of photo-excited electrons and hole pairs.

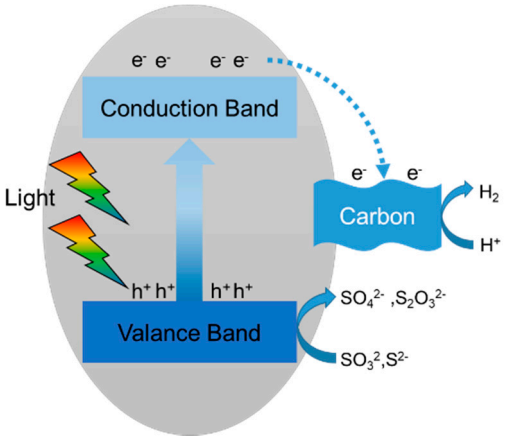

Figure 7. Photocatalytic process of H_2 formation in N-doped SiC.

3. Experimental

3.1. Chemicals and Materials

All the reagents used in this research were analytically pure and applied without further treatment. The raw materials used in the experiment mainly included fine silicon powder and carbon powder of 99.999% purity with a particle size of 5–10 μm and 5–20 μm, respectively.

3.2. Material Synthesis

The SiC powder was synthesized using the combustion method. The reactant silicon and carbon powder with a precisely controlled molar ratio of 1:1 were sealed into a PTFE milling tank to homogeneously mix for 24 h at room temperature. Then, the resulting mixture and 3 C–SiC powder (work as seed) were put into graphite crucibles and placed in a horizontal alumina tubular furnace which was procedurally heated to 1550 °C at a rate of 3 °C·min^{-1} and kept for 30 min. Then, the furnace was cooled to 800 °C at a same rate and naturally cooled down to room temperature. During the whole process of heating and cooling, nitrogen was continuously inflowed as the doping source at a flow rate of 400 sccm, producing N-doped SiC known as SiC–N_2. Moreover, a sample was prepared by the same procedure in Ar and labeled as SiC–Ar in order to make a comparison.

3.3. Material Characterizations

The crystalline phase and composition of obtained products was characterized by a D8 Advance X-ray diffractometer (D8 Advance, Bruker, Billerica, MA, USA) with Cu Kα radiation (λ = 1.54178 Å) at 40 kV and 40 mA. The lattice constant of as-prepared SiC samples was calculated by Jade 5.0 software. The chemical states and surface properties of the samples were determined by X-ray photoelectron spectroscopy (ESCALAB 250, Thermo Fisher Scientific, Waltham, MA, USA) with a monochromatic Al Kα as the excitation source. The optical properties of the samples were measured using a UV-Vis spectrophotometer (UV2250, Shimadzu, Kyoto, Japan), in which BaSO4 was used as a reflectance standard. The surface morphologies of the as-prepared samples were observed and characterized by SEM (S-4800 field emission, Hitachi, Tokyo, Japan) and HRTEM (JEM 2100, JEOL, Tokyo, Japan).

3.4. Photocatalytic Tests

The photocatalytic H_2-production measurement was performed in Labsolar-6 A system (Perfectlight Technology, Beijing, China), which consisted of a 300 mL Pyrex glass reaction cell connected to a closed gas circulation and evacuation system. In a typical reaction, the photoreaction solution included 100 mg of photocatalysts, 100 mL of deionized water containing 0.1 M Na_2 SO_3 and 0.1 M Na_2 S as sacrificial reagents. Continuous magnetic stirring was maintained at the bottom of the reactor during the entire experiment to maintain the photocatalysts in suspension. A 300 W Xe arc lamp was employed as a light source and kept 1 cm away from the top of the reactor with an average light intensity of 120 $mW{\cdot}cm^{-2}$. The reaction temperature was sustained at ambient temperature by a circular cooling water system during the whole photocatalytic process. The hydrogen evolved was sampled and analyzed by an online thermal conductivity detector using a gas chromatograph (shiweipxGC-7806, TCD, with Ar as carrier gas) every 1 h of illumination, which lasted for 5 h. A cyclic experiment repeated 3 times was carried out to determine the photocatalytic stability of the samples.

3.5. Photocurrent Test

Photocurrent measurements were conducted by an electrochemical workstation (CHI760, Chenhua Instrument, Shanghai, China), coupled with a Xe lamp (PLS-SXE300 UV, TrustTech, Beijing, China) using a standard three-electrode configuration with 0.5 M Na_2 SO_4 as electrolyte solution. The platinum plate (1.0 cm × 1.0 cm) electrode, the prepared samples photoelectrode, and a standard Ag–AgCl electrode were used as counter, working, and reference electrodes, respectively.

4. Conclusions

Solar-light-driven N-doped 3 C–SiC powder was synthesized via a simple one-step combustion route. It was apparent that the N-doping played a significant role in the crystallinity, phase transformation, optical, and photoelectrical properties of the SiC samples, which further affected the photoactivity. SiC–N_2 photocatalysts exhibited 205.3 μL/(g·h) hydrogen evolution rate, nearly twice that of SiC–Ar (120.1 μL/(g·h)), and much higher than that of SiC nanowires (83.9 μL/(g·h)), SiC nanoparticles (82.8 μL/(g·h)), as well as the B-doped SiC photocatalysts (166 μL/(g·h)). This suggested that the photocatalytic performance was primarily attributed to the enhancement of light-use ability by band-gap adjustment and carbon surface, efficient separation of photo-excited carriers through the interface, and the capture of hole traps, chemical activities resulting from defects and grain size, and the increased absorptivity caused by carbon, which was produced during the phase transformation. This work presents a simple method for meeting the requirements for durable and non-toxic catalysts at low cost.

Author Contributions: Conceptualization, W.L. and X.Y.; Formal analysis, W.L. and Q.L.; Data curation, W.L.; Writing—original draft, W.L.; Writing—review & editing, W.L.; Q.L.; X.Y.; X.C. and X.X.; Project administration, X.Y.; Funding acquisition, X.Y.; All authors have read and agreed to the published version of the manuscript.

Funding: This work was supported by "National Key R&D Program of China" under grants (2016YFB0400401). This work was supported by National Key R&D Program of China (Grant No. 2018 YFB0905701), the Key-area Research and Development Program of Guangdong Province (Grant No. 2019 B010126001), Youth Program of National Natural Science Foundation of China (Grant No. 51902182), Outstanding Youth Fund of Shandong Province (Grant No. ZR2019 JQ01), Natural Science Foundation of Shandong Province (Grant No. ZR2019 BEM011) and Fundamental Research Funds of Shandong University (Grant No. 2018 JCG01).

Conflicts of Interest: The authors declare no conflicts of interest.

References

1. Schloegl, R. Energy: Fuel for thought. *Nat. Mater.* **2008**, *7*, 772–774. [CrossRef] [PubMed]
2. Kudo, A.; Miseki, Y. Heterogeneous photocatalyst materials for water splitting. *Chem. Soc. Rev* **2009**, *38*, 253. [CrossRef]

3. Getoff, N. Photoelectrochemical and photocatalytic methods of hydrogen production: A short review. *Int. J. Hydrogen. Energy* **1990**, *15*, 407–417. [CrossRef]
4. Inoue, T.; Fujishima, A.; Konishi, S.; Honda, K. Photoelectrocatalytic reduction of carbon dioxide in aqueous suspensions of semiconductor powders. *Nature* **1979**, *277*, 637–638. [CrossRef]
5. Kudo, A. Recent progress in the development of visible light-driven powdered photocatalysts for water splitting. *Int. J. Hydrogen Energy* **2007**, *32*, 2673–2678. [CrossRef]
6. Abe, R. Recent progress on photocatalytic and photoelectrochemical water splitting under visible light irradiation. *J. Photochem. Photobio. C Photochem. Rev.* **2010**, *11*, 179–209. [CrossRef]
7. Li, X.; Yu, J.; Low, J.; Fang, Y.; Xiao, J.; Chen, X. Engineering heterogeneous semiconductors for solar water splitting. *J. Mat. Chem. A* **2015**, *3*, 2485–2534. [CrossRef]
8. Steenackers, M.; Sharp, I.D.; Larsson, K.; Hutter, N.A.; Stutzmann, M.; Jordan, R. Structured Polymer Brushes on Silicon Carbide. *Chem. Mat* **2010**, *22*, 272–278. [CrossRef]
9. Li, X.; Zhou, X.; Gao, Q.; Yuan, J.; Wen, J.; Fang, Y.; Liu, W.; Zhang, S.; Liu, Y. Metal-free carbon nanotube–SiC nanowire heterostructures with enhanced photocatalytic H_2 evolution under visible light irradiation. *Catal. Sci. Technol.* **2015**, *5*, 2798–2806.
10. Yang, J.; Zeng, X.; Chen, L.; Yuan, W. Photocatalytic water splitting to hydrogen production of reduced graphene oxide/SiC under visible light. *Appl. Phys. Lett.* **2013**, *102*, 83101. [CrossRef]
11. Wu, X.L.; Xiong, S.J.; Zhu, J.; Wang, J.; Shen, J.C.; Chu, P.K. Identification of surface structures on 3C-SiC nanocrystals with hydrogen and hydroxyl bonding by photoluminescence. *Nano Lett.* **2009**, *9*, 4053. [CrossRef] [PubMed]
12. Zhou, W.; Yan, L.; Wang, Y.; Zhang, Y. SiC nanowires: A photocatalytic nanomaterial. *Appl. Phys. Lett.* **2006**, *89*, 37. [CrossRef]
13. Liu, H.; She, G.; Mu, L.; Shi, W. Porous SiC nanowire arrays as stable photocatalyst for water splitting under UV irradiation. *Mat. Res. Bull.* **2012**, *47*, 917–920. [CrossRef]
14. Hao, J.Y.; Wang, Y.Y.; Tong, X.L.; Jin, G.Q.; Guo, X.Y. SiC nanomaterials with different morphologies for photocatalytic hydrogen production under visible light irradiation. *Catal. Today* **2013**, *212*, 220–224. [CrossRef]
15. Yang, T.; Chang, X.; Chen, J.; Chou, K.C.; Hou, X. B-doped 3C-SiC nanowires with a finned microstructure for efficient visible light-driven photocatalytic hydrogen production. *Nanoscale* **2015**, *7*, 8955–8961. [CrossRef]
16. Dong, L.L.; Wang, Y.Y.; Tong, X.L.; Jin, G.Q.; Guo, X.Y. Synthesis and Characterization of Boron-Doped SiC for Visible Light Driven Hydrogen Production. *Acta Phys.-Chim. Sin.* **2014**, *30*, 135–140.
17. Dang, H.; Li, B.; Li, C.; Zang, Y.; Xu, P.; Zhao, X.; Fan, H.; Qiu, Y. One-dimensional Au/SiC heterojunction nanocomposites with enhanced photocatalytic and photoelectrochemical performances: Kinetics and mechanism insights. *Electrochim. Acta* **2018**, *267*, 24–33. [CrossRef]
18. Wang, M.; Chen, J.; Liao, X.; Liu, Z.; Zhang, J.; Gao, L.; Li, Y. Highly efficient photocatalytic hydrogen production of platinum nanoparticle-decorated SiC nanowires under simulated sunlight irradiation. *Int. J. Hydrog. Energy* **2014**, *39*, 14581–14587. [CrossRef]
19. Wang, D.; Liu, N.; Guo, Z.; Wang, W.; Guo, L.; Yuan, W.; Chen, X. Hexagonal SiC with spatially separated active sites on polar and nonpolar facets achieving enhanced hydrogen production from photocatalytic water reduction. *Phys. Chem. Chem. Phys.* **2018**, *20*, 4787–4792. [CrossRef]
20. Mishra, G.; Parida, K.M.; Singh, S.K. Facile fabrication of S-TiO_2/β-SiC nanocomposite photocatalyst for hydrogen evolution under visible light irradiation. *ACS Sustain. Chem. Eng.* **2015**, *3*, 245–253. [CrossRef]
21. Zhou, X.; Liu, Y.; Li, X.; Gao, Q.; Liu, X.; Fang, Y. Topological morphology conversion towards SnO2/SiC hollow sphere nanochains with efficient photocatalytic hydrogen evolution. *Chem. Commun.* **2014**, *50*, 1070–1073. [CrossRef] [PubMed]
22. Guo, X.; Tong, X.; Wang, Y.; Chen, C.; Jin, G.; Guo, X.Y. High photoelectrocatalytic performance of a MoS2-SiC hybrid structure for hydrogen evolution reaction. *J. Mat. Chem. A* **2013**, *1*, 4657–4661. [CrossRef]
23. Peng, Y.; Guo, Z.; Yang, J.; Wang, D.; Yuan, W. Enhanced photocatalytic H_2 evolution over micro-SiC by coupling with CdS under visible light irradiation. *J. Mat. Chem. A* **2014**, *2*, 6296–6300. [CrossRef]
24. Peng, Y.; Guo, Z.; Wang, D.; Pan, N.; Yuan, W. Heterogeneous nucleation of CdS to enhance visible-light photocatalytic hydrogen evolution of SiC/CdS composite. *Appl. Phys. Lett.* **2015**, *107*, 37. [CrossRef]

25. Peng, Y.; Han, G.; Wang, D.; Wang, K.; Guo, Z.; Yang, J.; Yuan, W. Improved H_2 evolution under visible light in heterostructured SiC/CdS photocatalyst: Effect of lattice match. *Int. J. Hydrog. Energy* **2017**, *42*, 14409–14417. [CrossRef]
26. Wang, B.; Zhang, J.; Huang, F. Enhanced visible light photocatalytic H_2 evolution of metal-free g-C_3N_4 /SiC heterostructured photocatalysts. *Appl. Surf. Sci.* **2016**, *391*, 449–456. [CrossRef]
27. Wang, D.; Guo, Z.; Yuan, P.; Yuan, W. A simple route to significant enhancement of photocatalytic water oxidation on $BiVO_4$ by heterojunction with SiC. *Chem. Eng. J.* **2015**, *281*, 102–108. [CrossRef]
28. Gong, Y.; Jiang, P.G.; Wang, Y.X.; Wu, T.; Lin, J.H. Enhanced photocatalytic performance of chemically bonded SiC-graphene composites for visible-light-driven overall water splitting. *Int. J. Hydrog. Energy* **2013**, *38*, 12733–12738.
29. Zhu, K.; Guo, L.; Lin, J.; Hao, W.; Shang, J.; Jia, Y.; Chen, L.; Jin, S.; Wang, W.; Chen, X. Graphene covered SiC powder as advanced photocatalytic material. *Appl. Phys. Lett.* **2012**, *100*, 197. [CrossRef]
30. Lu, W.; Wang, D.; Guo, L.; Jia, Y.; Ye, M.; Huang, J.; Li, Z.; Peng, Y.; Yuan, W.; Chen, X. Bipolar Carrier Transfer Channels in Epitaxial Graphene/SiC Core-Shell Heterojunction for Efficient Photocatalytic Hydrogen Evolution. *Adv. Mat.* **2015**, *27*, 7986–7991. [CrossRef]
31. Zhou, X.; Gao, Q.; Li, X.; Liu, Y.; Zhang, S.; Fang, Y.; Li, J. Ultra-thin SiC Layers Covered Graphene Nanosheets as Advanced Photocatalysts for Hydrogen Evolution. *J. Mat. Chem. A* **2015**, *3*, 10999–11005. [CrossRef]
32. Cui, Y.; Hu, X.; Yang, K.; Yang, X.; Xie, X.; Xiao, L.; Xu, X. Influence of Nitrogen Concentrations on the Lattice Constants and Resistivities of n-Type 4H-SiC Single Crystals. *Cryst. Growth Des.* **2015**, *15*, 3131–3136. [CrossRef]
33. Li, Z.; Zhou, W.; Luo, F.; Huang, Y.; Li, G.; Su, X. Improving the dielectric properties of SiC powder through nitrogen doping. *Mat. Sci. Eng. B* **2011**, *176*, 942–944. [CrossRef]
34. Wang, M.J.; Wada, H. Synthesis and characterization of silicon nitride whiskers. *J. Mat. Sci.* **1990**, *25*, 1690–1698. [CrossRef]
35. Choi, J.Y.; Chong, H.K.; Kim, D.K. Carbothermic Synthesis of Monodispersed Spherical Si3N4/SiC Nanocomposite Powder. *J. Am. Ceram. Soc.* **1999**, *82*, 2665–2671. [CrossRef]
36. Liu, H.S.; Fang, X.Y.; Song, W.L.; Hou, Z.L.; Cao, M.S. Modification of Band Gap of beta-SiC by N-Doping. *Chin. Phys. Lett.* **2009**, *26*, 237–240.
37. Ténégal, F.; de la Rocque, A.G.; Dufour, G.; Sénémaud, C.; Doucey, B.; Bahloul-Hourlier, D.; Goursat, P.; Mayne, M.; Cauchetier, M. Structural determination of sintered Si3N4/SiC nanocomposite using the XPS differential charge effect. *J. Electron. Spectrosc. Relat. Phenom.* **2000**, *109*, 241–248. [CrossRef]
38. Ito, S.; Murata, T.; Hasegawa, M.; Bito, Y.; Toyoguchi, Y. Anode Materials C xN with Graphite-like Structure for Secondary Lithium Batteries. *Denki Kagaku* **1996**, *64*, 1180–1184. [CrossRef]
39. Smirnova, T.P.; Badalian, A.M.; Yakovkina, L.V.; Kaichev, V.V.; Bukhtiyarov, V.I.; Shmakov, A.N.; Asanov, I.P.; Rachlin, V.I.; Fomina, A.N. SiCN alloys obtained by remote plasma chemical vapour deposition from novel precursors. *Thin Solid Films* **2003**, *429*, 144–151. [CrossRef]
40. Cho, W.S.; Oh, Y.S.; Kim, C.S.; Osada, M.; Kakihana, M.; Lim, D.S.; Cheong, D.S. Characterization of Si3N4/SiC nanocomposite by Raman scattering and XPS. *J. Alloy. Compd.* **1999**, *285*, 255–259. [CrossRef]
41. Oh, Y.S.; Cho, W.S.; Kim, C.S.; Lim, D.S.; Cheong, D.S. XPS Investigation of Si3N4/SiC Nanocomposites Prepared Using a Commercial Polymer. *J. Am. Ceram. Soc.* **1999**, *82*, 927–932. [CrossRef]
42. Avila, J.; Sacedon, J.L. Reactivity at the Al/Si3N4 interfaces. *Appl. Phys. Lett.* **1995**, *66*, 757–759. [CrossRef]
43. Makuła, P.; Pacia, M.; Macyk, W. How To Correctly Determine the Band Gap Energy of Modified Semiconductor Photocatalysts Based on UV–Vis Spectra. *J. Phys. Chem. Lett.* **2018**, *9*, 6814–6817. [CrossRef] [PubMed]